

Stimulated X-ray Raman and Absorption Spectroscopy of Iron–Sulfur Dimers

Daeheum Cho,^{*,†,‡} Jeremy R. Rouxel,^{†,‡} Shaul Mukamel,^{*,†,‡} Garnet Kin-Lic Chan,^{*,‡} and Zhendong Li^{*,‡,§}

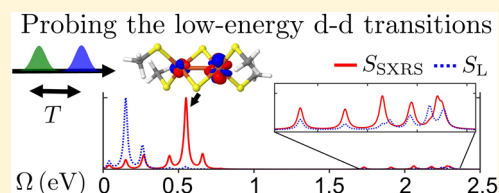
[†]Department of Chemistry and Physics and Astronomy, University of California, Irvine, California 92697-2025, United States

[‡]Division of Chemistry and Chemical Engineering, California Institute of Technology, Pasadena, California 91125, United States

[§]Key Laboratory of Theoretical and Computational Photochemistry, Ministry of Education, College of Chemistry, Beijing Normal University, Beijing 100875, China

S Supporting Information

ABSTRACT: Iron–sulfur complexes play an important role in biological processes such as metabolic electron transport. A detailed understanding of the mechanism of long-range electron transfer requires knowledge of the electronic structure of the complexes, which has traditionally been challenging to obtain, either by theory or by experiment, but the situation has begun to change with advances in quantum chemical methods and intense free electron laser light sources. We compute the spectra for stimulated X-ray Raman spectroscopy (SXRS) and absorption spectroscopy of homovalent and mixed-valence [2Fe–2S] complexes, using the *ab initio* density matrix renormalization group algorithm. The simulated spectra show clear signatures of the theoretically predicted dense low-lying excited states within the d–d manifold. Furthermore, the difference in spectral intensity between the absorption-active and Raman-active states provides a potential mechanism to selectively excite states by a proper tuning of the excitation pump, to access the electronic dynamics within this manifold.



Iron–sulfur (Fe–S) complexes are pervasive in Nature.^{1–3} The most common motifs include the [2Fe–2S] and [4Fe–4S] clusters contained in ferredoxin (Fd) proteins, which mediate electron transfer in many metabolic reactions. During electron transfer, the [2Fe–2S] clusters convert between the homovalent [2Fe(III,III)–2S] and mixed-valence [2Fe(III,II)–2S] forms upon receiving or donating electrons. However, unlike in many other biological systems, the detailed mechanism of electron transfer involving Fe–S clusters is not well understood at the molecular level. This is often attributed to the rather complicated electronic structure of these clusters.⁴ Spectroscopic and magnetic susceptibility studies^{5–8} established early on that in these complexes, each iron atom can be formally viewed as a high-spin ferric iron with $S = 5/2$ or ferrous iron with $S = 2$, coordinated to four sulfur atoms (either from the thiolate or bridge sulfide) in a (distorted) tetrahedral environment. The ground states of these Fe–S clusters are formed by antiferromagnetically coupled Fe(III)–Fe(III) and Fe(III)–Fe(II) pairs, respectively, which leads to a diamagnetic $S = 0$ state for the homovalent dimer and a $S = 1/2$ state for the mixed-valence dimer which has a clear electron paramagnetic resonance (EPR) signature.^{5,6} Similar electronic features have been widely observed in a variety of synthetic analogs of [2Fe–2S] clusters.^{9–11} While these basic features can be described by the Heisenberg double exchange model^{12,13} in combination with broken-symmetry density functional theory (BS-DFT),^{14–17} more recent theoretical work^{18,19} has shown that the excited state spectrum is much

more involved and cannot be described by this simple approach. Instead, using the *ab initio* density matrix renormalization group (DMRG) algorithm,^{20–24} it has been shown that the low-energy spectrum is very dense due to the presence of a large number of d–d excited states arising from both orbital transitions and spin recouplings.¹⁸ Indirect experimental evidence of the dense low-energy manifold has recently been obtained using iron L-edge 2p3d resonant inelastic X-ray scattering (RIXS).²⁵

In general, experimental access to the low-lying electronic excited states of [2Fe–2S] dimers through optical absorption is difficult, because d–d ligand-field excitations are essentially electric-dipole forbidden²⁶ as in mononuclear Fe–S complexes. In this work, we explore the use of nonlinear optical spectroscopies to probe the low-lying spectra of [2Fe–2S] dimers. Specifically, we simulate the spectra for the stimulated X-ray Raman spectroscopy (SXRS) of the homovalent and mixed-valence [2Fe–2S] complexes and compare them to simulated absorption spectra, using electronic excited states computed with the *ab initio* DMRG technique. Stimulated X-ray Raman techniques have been a source of growing interest over the past years, and will provide insights on matter degrees of freedom otherwise inaccessible.^{27–32} We find that the

Received: August 16, 2019

Accepted: September 18, 2019

Published: September 18, 2019

absorption and SXRS techniques complement each other by accessing different parts of the electronic spectrum and together can effectively probe the dense d–d electronic states in the Fe–S clusters. Thanks to the availability of accurate many-electron wave functions from DMRG, a detailed assignment of the spectra then becomes possible, to aid the understanding of experimental spectroscopy of iron–sulfur dimers in the future.

Simulation of Stimulated X-ray Raman (SXRS) Spectra. We shall calculate the stimulated X-ray Raman spectra using the minimal coupling Hamiltonian rather than the multipolar Hamiltonian. SXRS has some similarities with the well-established RIXS. Both SXRS and RIXS rely on an inelastic scattering process (Raman process) of X-ray beams. However, RIXS is always resonant to ensure element sensitivity^{33–35} while off-resonant SXRS also offers interesting information on the valence excited manifold. Moreover, RIXS is measured in the homodyne (spontaneous) detection mode while SXRS is heterodyne-detected. In atomic units, the minimal coupling field-matter interaction Hamiltonian is given by³⁶

$$\hat{H}_{\text{int}}(t) = - \int d\mathbf{r} \hat{\mathbf{j}}(\mathbf{r}) \cdot \hat{\mathbf{A}}(\mathbf{r}) + \frac{1}{2} \int d\mathbf{r} \hat{\sigma}(\mathbf{r}) \hat{\mathbf{A}}^2(\mathbf{r}) \quad (1)$$

where $\hat{\mathbf{j}}(\mathbf{r})$ and $\hat{\sigma}(\mathbf{r})$ are the current and charge density operators, respectively, and $\hat{\mathbf{A}}(\mathbf{r})$ is the vector potential. The current $\hat{\mathbf{j}}(\mathbf{r})$ and charge density $\hat{\sigma}(\mathbf{r})$ operators are defined as

$$\hat{\mathbf{j}}(\mathbf{r}) = \frac{1}{2i} (\hat{\psi}^\dagger(\mathbf{r}) \nabla \hat{\psi}(\mathbf{r}) - (\nabla \hat{\psi}^\dagger(\mathbf{r})) \hat{\psi}(\mathbf{r})) \quad (2)$$

$$\hat{\sigma}(\mathbf{r}) = \hat{\psi}^\dagger(\mathbf{r}) \hat{\psi}(\mathbf{r}) \quad (3)$$

where $\hat{\psi}^{(\dagger)}(\mathbf{r})$ is the electron field annihilation (creation) operator, which satisfies the Fermi anticommutation relation $\{\hat{\psi}(\mathbf{r}), \hat{\psi}^\dagger(\mathbf{r}')\} = \delta(\mathbf{r} - \mathbf{r}')$. The vector potential is written as a field mode expansion

$$\hat{\mathbf{A}}(\mathbf{r}) = \sum_{\mathbf{k}, \lambda_j} \sqrt{\frac{2\pi}{\Omega\omega_j}} (\epsilon^{(\lambda_j)}(\mathbf{k}_j) \hat{a}_j e^{i\mathbf{k}_j \cdot \mathbf{r}} + \epsilon^{(\lambda_j)*}(\mathbf{k}_j) \hat{a}_j^\dagger e^{-i\mathbf{k}_j \cdot \mathbf{r}}) \quad (4)$$

where $\hat{a}_j^{(\dagger)}$ is the photon field boson annihilation (creation) operator for mode j , Ω the field quantization volume, and $\epsilon^{(\lambda_j)}(\mathbf{k}_j)$ the polarization vector. In the minimal-coupling Hamiltonian, the exact light–matter coupling can be obtained by the substitution $\hat{\mathbf{p}} \rightarrow \hat{\mathbf{p}} - e\hat{\mathbf{A}}$, where $\hat{\mathbf{p}}$ is the electronic momentum operator. The matter property enters through the current $\hat{\mathbf{j}}(\mathbf{r})$ and charge density $\hat{\sigma}(\mathbf{r})$ operators, and the light property through the vector potential $\hat{\mathbf{A}}$. In this formalism, an off-resonant Raman process is described by the transition charge density (TCD) $\sigma_{ij}(\mathbf{r})$, which can be calculated as a transition property between the states i and j . A resonant transition is described by the transition current density $j_{ij}(\mathbf{r})$. In the multipolar Hamiltonian, however, the off-resonant Raman transition between the states i and j is described by the transition polarizability α_{ij} , which requires additional computational cost to sum over all the relevant intermediate electronic states k . The minimal-coupling Hamiltonian approach is, therefore, more suitable for the calculation of an off-resonant Raman process than the multipolar Hamiltonian. Simulation of hard X-ray spectroscopy also requires a description of the spatial variation of the field across the molecular sample, and this is also most suited to being calculated in the minimal-coupling formalism.

In the setup shown in Figure 1, two X-ray or UV pulses with a controlled delay T are incident on a sample (Figure 1a) and

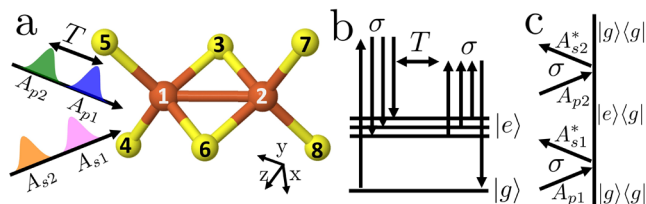


Figure 1. (a) Sketch of the pulse configuration relative to the [2Fe–2S] complex. (b) Level diagrams representing the process. $|g\rangle$ and $|e\rangle$ are the ground and valence excited states. (c) Ladder diagram of the signal.

induce two Raman processes (Figure 1b). The signal is measured as a function of T and then Fourier transformed to obtain a spectrum, which reveals the valence manifold. Figure 1c gives the ladder diagram of the signal.

By neglect of the $\mathbf{j} \cdot \mathbf{A}$ term, which dominates resonant scattering, the off-resonant heterodyne signal is defined as the time-integrated rate of change of photon number of the field mode occupied by the heterodyne pulse A_{s2} (Figure 1c)

$$S_{\text{SXRS}} = \int dt \left\langle \frac{d}{dt} \hat{N}_{s2}(t) \right\rangle \quad (5)$$

where the number operator for the photon mode with heterodyne field $\hat{N}_{s2} = a_{s2}^\dagger a_{s2}$ and $a_{s2}^{(\dagger)}$ is a photon annihilation (creation) operator in the $s2$ field mode. Computing the commutator $[\hat{H}_{\text{int}}, \hat{N}_{s2}]$ then gives the signal as

$$S_{\text{SXRS}}(\mathbf{k}_s) = 2\mathcal{T} \int d\mathbf{r} dt \langle \hat{\sigma}(\mathbf{r}, t) \rangle A_{s2}^*(\mathbf{r}, t) \cdot A_{p2}(\mathbf{r}, t) \quad (6)$$

where \mathbf{k}_s is the wavevector of the signal field. $A_{p2}(\mathbf{r}, t)$ and $A_{s2}^*(\mathbf{r}, t)$ are the probe field and its scattered field, respectively, as shown in Figure 1c. Similarly, the pump fields to create a $|g\rangle\langle e|$ coherence are labeled $A_{p1}(\mathbf{r}, t)$ and $A_{s1}^*(\mathbf{r}, t)$ as in the figure. The off-resonant SXRS is obtained by expanding eq 6 to second order in σA^2 and keeping the terms corresponding to the process in Figure 1c,

$$S_{\text{SXRS}}(\mathbf{k}_s) = 2\mathcal{T} \times \int d\mathbf{r}_2 d\mathbf{r}_1 dt_2 dt_1 \langle \hat{\sigma}(\mathbf{r}_2, t_2) \hat{\sigma}(\mathbf{r}_1, t_1) \rangle \times A_{s2}^*(\mathbf{r}_2, t_2) \cdot A_{p2}(\mathbf{r}_2, t_2) A_{s1}^*(\mathbf{r}_1, t_1) \cdot A_{p1}(\mathbf{r}_1, t_1) \quad (7)$$

The incoming fields have a plane wave form $A_{pi}(\mathbf{r}_i, t_i) = \mathcal{A}_{pi} \epsilon_i e^{i(\mathbf{k}_{pi} \cdot \mathbf{r}_i - \omega_{pi} t_i)}$ where \mathcal{A}_{pi} is the field amplitude, ϵ_i its polarization, \mathbf{k}_{pi} its wavevector, and ω_{pi} its frequency. The spectra are computed for the X, Y, and Z incoming pulse directions. The two-point correlation function of charge densities in eq 7, $\langle \hat{\sigma}(\mathbf{r}_2, t_2) \hat{\sigma}(\mathbf{r}_1, t_1) \rangle$ can be dissected into two contributions: a two-molecule contribution and a one-molecule one. The first term gives rise to a structure factor as a prefactor that vanishes in the absence of order. The one-molecule contribution does not vanish upon rotational averaging and is the expression used for gas, liquid phase, or single molecule scattering. Note that our simulations will assume an oriented single molecule (the relative orientation with the fields is shown in Figure 1a). This single-molecule orientation in the gas phase may be prepared by an extra aligning pulse prior to an SXRS measurement. To describe gas

Table 1. Vertical Excitation Energies for the Lowest 19 Excited States ω_{eg} (eV) for Fe(III)–Fe(III) ($S = 0$) and Fe(III)–Fe(II) ($S = 1/2$) Dimers from State-Averaged DMRG^a

complex	state									
	1	2	3	4	5	6	7	8	9	10
Fe(III)–Fe(III)	11	12	13	14	15	16	17	18	19	
	2.06	2.21	2.33	2.44	2.45	2.53	2.63	2.66	2.75	2.80
	(0.54)	(0.63)	(0.62)	(0.64)	(0.66)	(0.68)	(0.65)	(0.66)	(0.62)	(0.60)
	2.88	2.94	2.97	3.01	3.05	3.12	3.13	3.16	3.18	
Fe(III)–Fe(II)	(0.62)	(0.62)	(0.67)	(0.58)	(0.62)	(0.65)	(0.66)	(0.54)	(0.62)	
	0.04	0.15	0.26	0.27	0.44	0.53	0.55	0.66	0.78	1.73
	(0.45)	(0.47)	(0.46)	(0.53)	(0.47)	(0.61)	(0.64)	(0.26)	(0.34)	(0.24)
	1.91	2.06	2.09	2.17	2.18	2.25	2.28	2.30	2.31	
	(0.07)	(0.23)	(0.38)	(0.20)	(0.06)	(0.11)	(0.18)	(0.11)	(0.38)	

^aThe values in parentheses correspond to $\text{tr}[\gamma^\dagger \gamma]$, where γ is the transition density matrix. The deviation from one can be regarded as a signature that the excitation involves multiple (instead of single) excitation character.

or liquid phase signals without molecular ordering, rotational averaging should otherwise be performed. Some structural information will be lost upon rotational averaging over such randomly oriented molecules, but the main spectral features should be similar.

After expanding the matter correlation function in eigenstates, assuming that all incoming pulses have the same polarization we obtain

$$S_{\text{SXRS}}(\Omega) = 2\mathcal{J} \sum_{\mathbf{e}} \left(\frac{\sigma_{\text{ge}}(\mathbf{q}_2) \sigma_{\text{eg}}(\mathbf{q}_1)}{\Omega - \omega_{\text{eg}} - i\Gamma_{\text{eg}}} + \frac{\sigma_{\text{ge}}(-\mathbf{q}_2) \sigma_{\text{eg}}(-\mathbf{q}_1)}{\Omega + \omega_{\text{eg}} - i\Gamma_{\text{eg}}} \right) \quad (8)$$

where Ω is the Fourier variable conjugate to the time delay T , $\sigma_{\text{ge}}(\mathbf{q})$ is the Fourier transform of the transition charge density $\sigma_{\text{ge}}(\mathbf{r})$, the momentum transfer $\mathbf{q}_i = \mathbf{k}_{\text{si}} - \mathbf{k}_{\text{pi}}$ and the dephasing rate $\Gamma_{\text{eg}} = 0.014$ eV. In the long wavelength limit we have

$$\begin{aligned} \sigma_{\text{eg}}(\mathbf{q}_i) &= \int e^{i\mathbf{k}_{\text{si}} \cdot \mathbf{r}} e^{-i\mathbf{k}_{\text{pi}} \cdot \mathbf{r}} \sigma_{\text{eg}}(\mathbf{r}) d\mathbf{r} \\ &= \int \sigma_{\text{eg}}(\mathbf{r}) (1 + i\mathbf{k}_{\text{si}} \cdot \mathbf{r})(1 - i\mathbf{k}_{\text{pi}} \cdot \mathbf{r}) \\ &= \int \sigma_{\text{eg}}(\mathbf{r}) d\mathbf{r} + i \int (\mathbf{k}_{\text{si}} - \mathbf{k}_{\text{pi}}) \cdot \mathbf{r} \sigma_{\text{eg}}(\mathbf{r}) d\mathbf{r} \\ &\quad + \int d\mathbf{r} (\mathbf{k}_{\text{si}} \cdot \mathbf{r})(\mathbf{k}_{\text{pi}} \cdot \mathbf{r}) \sigma_{\text{eg}}(\mathbf{r}) \end{aligned} \quad (9)$$

The first term vanishes by the definition of the transition charge density. The magnitude of the difference between the in the second term $(\mathbf{k}_{\text{si}} - \mathbf{k}_{\text{pi}})$ is small compared to that of the product appearing in the last term $(\mathbf{k}_{\text{si}} \cdot \mathbf{k}_{\text{pi}})$ and can thus be neglected. We then obtain for the effective transition charge density.

$$\alpha_{\text{eg}} = \omega_{\text{si}} \omega_{\text{pi}} \int (\epsilon_{\text{si}} \cdot \mathbf{r})(\epsilon_{\text{pi}} \cdot \mathbf{r}) \sigma_{\text{eg}}(\mathbf{r}) d\mathbf{r} \quad (10)$$

where ϵ_{si} and ϵ_{pi} are the direction of propagation of the i th probe and the scattered fields, respectively. The effective TCD α_{eg} no longer depends on \mathbf{r} since we have made the long-wavelength approximation. The signal in eq 8 is given by

$$S_{\text{SXRS}}(\Omega) = 2\mathcal{J} \sum_{\mathbf{e}} \left(\frac{\alpha_{\text{ge}} \alpha_{\text{eg}}}{\Omega - \omega_{\text{eg}} - i\Gamma_{\text{eg}}} + \frac{\alpha_{\text{ge}} \alpha_{\text{eg}}}{\Omega + \omega_{\text{eg}} - i\Gamma_{\text{eg}}} \right) \quad (11)$$

In this paper, we take all the pulse propagation axes ϵ_{si} and ϵ_{pi} the same for the SXRS signal, either X , Y , or Z axis shown in Figure 1.

The absorption spectrum S_{L} was calculated from the transition dipole moment μ_{eg} between states g and e , transition frequency ω_{eg} and the dephasing rate $\Gamma_{\text{eg}} = 0.014$ eV

$$S_{\text{L}}(\omega) = \sum_{\mathbf{e}} \frac{|\mu_{\text{eg}}|^2 \Gamma_{\text{eg}}}{(\omega - \omega_{\text{eg}})^2 + \Gamma_{\text{eg}}^2} \quad (12)$$

Computational Methods for the Electronic Excited States of [2Fe–2S] Complexes. The computation of the electronic structure of Fe–S complexes is challenging due to the presence of many nearly degenerate d orbitals. A minimal active space for the ground state, which includes the 3d orbitals of Fe and 3p orbitals of the bridging S (to qualitatively capture double exchange³⁷) already contains 16 orbitals, which approaches the limit of traditional multireference methods. To more accurately describe the low-lying excited states by allowing for the effects of d-electron orbital relaxation, a second set of d-shell orbitals³⁸ was added into the active space, along with two 4s orbitals as in previous work.¹⁸ In addition, the eight terminal thiolate p orbitals (one σ and π each¹⁹) were included as well. This gives rise to complete active space (CAS) models of size CAS(38e,36o) for the ferric–ferric dimer and CAS(39e,36o) for the ferric–ferrous dimer. These are expanded from the previously employed active spaces in ref 18 by the four π orbitals from the thiolates, which are included here so as to allow for possible ligand-to-metal charge-transfer (LMCT) in the excitations. Note that because empty sulfur orbitals are not included, our active space model excludes metal-to-ligand charge-transfer (MLCT) from Fe to S. However, the energies of such excited states are very high (ca. $>150\,000\text{ cm}^{-1}$)¹⁹ and thus do not contribute to the low-lying spectra investigated in this work. Thus, the current active space may be considered to provide a qualitative model of the low-lying excited states, capturing both the d–d as well as low-lying LMCT transitions, which both appear in the low-energy spectra of Fe–S complexes. While further inclusion of dynamic correlation is desirable,^{39,40} using the current active spaces in conjunction with computing many excited states already results in challenging calculations. We expect the use of a large active space will reduce the sensitivity of the simulated spectra with respect to the inclusion of dynamic correlation; however, this will be a topic for future study.

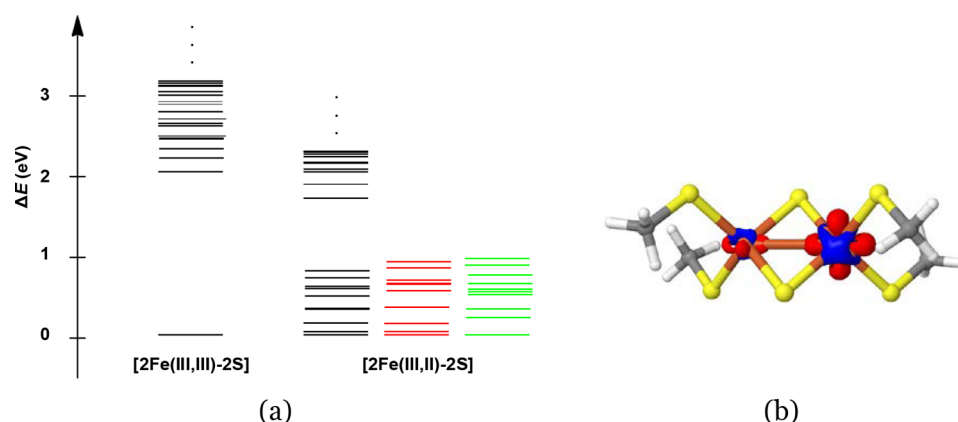


Figure 2. (a) Relative energies of the 20 low-lying electronic states of the ferric–ferric dimer with $S = 0$ (left) and the ferric–ferrous (right) dimer with $S = 1/2$. For comparison, the relative energies obtained in the previous work (ref 18) were also shown (red, unrelaxed geometry; green, relaxed geometry). (b) Charge density difference between the ferric–ferrous dimer and the ferric–ferric dimer, which illustrates the distribution of the excess electron.

While our previous study¹⁸ mostly focused on the lowest 10 states of the mixed-valence dimer, to access a larger part of the electronic spectrum, we computed 20 electronic states (1 ground state + 19 excited states of the same spin) for each dimer in this work using state-averaged DMRG with the above enlarged active space and some other additional improvements described below. The model complexes for the $[2\text{Fe}–2\text{S}]$ clusters were the same as used previously^{18,19} and were obtained from the synthetic complex of Mayerle et al.^{9,10} with the terminal groups simplified to methyl groups in order to reduce computational cost. The protocol for preparing active space orbitals described in ref 41 was employed in this work. This is based on split-localization (using Pipek–Mezey (PM) localization⁴²) of the unrestricted natural orbitals (UNOs) obtained from high-spin unrestricted Kohn–Sham (UKS) calculations using the BP86^{43,44} functional. Scalar relativistic effects were taken into account by the spin-free exact two-component (sf-X2C) Hamiltonian,^{45–48} and the cc-pVTZ-DK basis⁴⁹ was employed for all atoms. All of these calculations were performed with the PySCF package.⁵⁰ The resulting active orbitals are visualized in section 1 in the [Supporting Information](#). The subsequent state-averaged DMRG calculations were performed with the BLOCK code.²⁴ Most of the results (vertical excitation energies, charge and spin densities, and transition density matrices) presented in this paper were obtained from data corresponding to a (spin-adapted) bond dimension $D = 2000$. The vertical excitation energies for the lowest 19 excited states ω_{eg} (eV) for the $\text{Fe(III)}–\text{Fe(III)}$ dimer with $S = 0$ and the $\text{Fe(III)}–\text{Fe(II)}$ dimer with $S = 1/2$ are summarized in [Table 1](#) and [Figure 2a](#). DMRG calculations averaging over many states are computationally very expensive. To estimate the errors in our calculations, we compared the results at $D = 2000$ with a calculation with larger bond dimension $D = 3000$ (only performing 2 sweeps due to the computational cost). Because of the variational nature of DMRG, a lower energy (for a given state) means better convergence than a higher energy. For the first 9 excited states, on average, the change in excitation energies was -0.05 and -0.02 eV for the $[2\text{Fe(III,III)}–2\text{S}]$ and $[2\text{Fe(III,II)}–2\text{S}]$ complexes, respectively. For the next 10 higher energy excited states, the average changes were larger (-0.28 and -0.23 eV, respectively) although the qualitative features of the states remained unchanged. As shown in [Figure 2a](#), our results for the

relative energies of the lowest 10 states of the mixed-valence dimer are in agreement with our previous results.¹⁸

Nature of the Low-Lying Excited States. Before presenting the simulated spectra, we first analyze the nature of the low-lying excited states, which gives some basic insight into the electronic structure of the low-lying states. [Figure 2a](#) reveals that for the ferric–ferric dimer, there is a single dense band around 2–3 eV formed by the first 19 excited states, whereas for the ferric–ferrous dimer, the computed excited states split into two bands. The first 10 states (including the ground state) form a single band within 0.78 eV, while the next band formed by the rest of the states starts from 1.73 eV.

To analyze the excited states, in [Table 1](#), the values of $\text{tr}[\gamma^\dagger\gamma]$, where γ is the one-particle transition density matrix defined as $(\gamma_{\text{ge}})_{pq} = \langle \Psi_{\text{g}} | a_p^\dagger a_q | \Psi_{\text{e}} \rangle$, are listed for each excited state. Significant deviation of this value from one is a sign that multiple (instead of single) excitations are involved in $|\Psi_{\text{e}}\rangle$.^{51–53} (In the single-reference case, the above statement is exactly true, because if Ψ_{g} is described by a Slater determinant and $|\Psi_{\text{e}}\rangle$ is described at the level of CIS (configuration interaction singles), the corresponding value is precisely one, i.e., $\text{tr}[\gamma^\dagger\gamma] = 1$.) As shown in [Table 1](#), a common feature for the low-lying excited states in both Fe–S clusters is that they all contain substantial multiple excitation character. In particular, the excited states in the second band of the ferric–ferrous dimer can even be considered to be dominated by multiple excitations, which is also the case for the eighth and ninth excited states in the first band.

The origin of the excited states can be analyzed by visualizing the charge density differences between the excited states and the ground state shown in [Figures S2 and S3](#). For the ferric–ferric dimer, [Figure S2](#) shows the deletion of electron density on the bridge sulfur orbitals and the rearrangement of electron density on the two Fe ions. This indicates that the dense band of excited states for the ferric–ferric dimer can be attributed to a strong mixture of d–d excitations and LMCT from the bridging sulfur to the Fe ions. In contrast, for the reduced dimer, [Figure S3](#) reveals that the excited states are mainly composed of d–d excitations. Only very few of them involve a small amount of LMCT (e.g., see the 10th, 11th, 14th, 15th, and 19th states in [Figure S3](#)).

The exact nature of the d–d excitations is very hard to discern due to the heavy mixture of different types of single

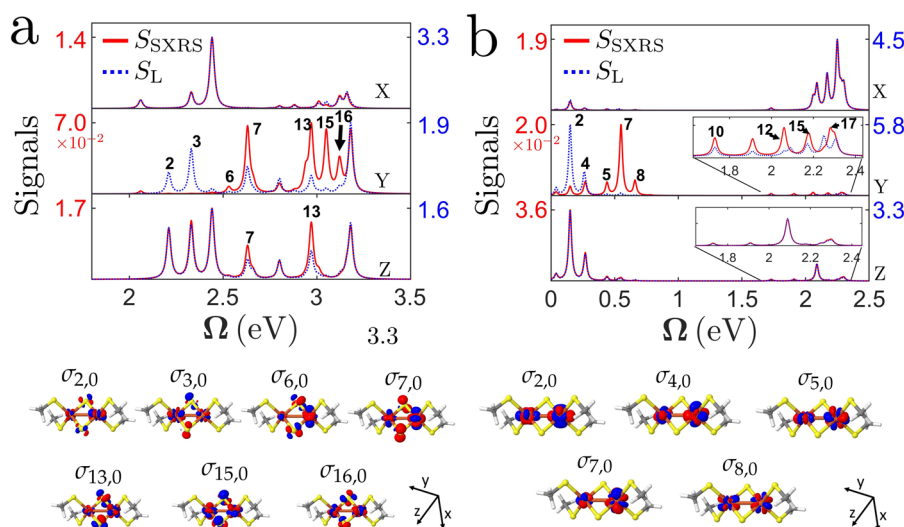


Figure 3. (a) SXRS spectra S_{SXRS} (eq 11, solid line) and absorption spectra S_L (eq 12, dashed line) of (a) Fe(III)–Fe(III) and (b) Fe(III)–Fe(II) dimers. (Top) Calculated spectra from X, Y, and Z polarized light. (See bottom of (b) for the axes). (Bottom) Selected TCDs are shown. $\Gamma_{\text{eg}} = 0.014$ eV for all states. Note that the absorption and SXRS spectra are normalized. Consequently, the strength of each spectroscopy in different directions can be compared, but SXRS and absorption strengths cannot be directly compared.

and multiple d–d excitations in the iron–sulfur dimers. There can be (A) local d–d excitations within one center, (B) simultaneous local d–d excitations on both centers, (C) charge-transfer d–d excitations between two centers, and multiple excitations with mixed character. Both types A and C of d–d excitations can either be single or multiple transitions, whereas the other types are multiple excitations by definition. From the charge density difference alone, it is difficult to trace the structure of the d–d excitations in the computed excited states to these different classes. Fortunately, for the purpose of understanding the spectroscopies shown below, it suffices to focus on the most relevant quantity, the TCD shown in Figure S4, for which only single excitations (types A and C) are relevant. To obtain more compact information, we decompose the transition density matrix γ using a singular value decomposition, $\gamma = \mathbf{U}\mathbf{A}\mathbf{V}^\dagger$ in a way similar to the definition of natural transition orbitals (NTO) in the case of CIS.⁵⁴ The resulting pairs of orbitals are referred to as binatural orbitals in the multireference context.⁵⁵ For simplicity, the two sets of orbitals defined by \mathbf{U} and \mathbf{V} will be denoted hole NTO (HNTO) and electron NTO (ENTO), respectively. The contribution of each pair of HNTO and ENTO to the transition density matrix is given by the singular value λ_k . However, as mentioned above, in the multireference case, one usually finds $\text{tr}[\gamma^\dagger\gamma] = \text{tr}(\mathbf{A}^\dagger\mathbf{A}) = \sum_k \lambda_k^2 < 1$. Thus, when discussing the contributions of each pair of HNTO and ENTO to the total TCD, we will use the normalized percentage $\lambda_k^2 / \sum_l \lambda_l^2$ (see Figures S5 and S6 in the Supporting Information). By analyzing the pairs of NTOs, we can interpret the character of the electronic transition contributing to the TCDs in a compact way.

Figure S5 shows the HNTOs and ENTOs for the ferric–ferric dimer. We find that the TCDs (see Figure S4a) for all excited states are mostly contributed by LMCT and d–d excitations with both local and charge-transfer character. This is consistent with the findings from analyzing charge density differences and the observation that the low-lying excited states in this complex contain a relatively larger amount of single excitation character than multiple excitation character (see

Table 1). For the ferric–ferrous case, Figure S6 shows that the TCDs (see Figure S4b) of the first band of excited states are purely due to local d–d excitations, viz., mostly $d(\text{Fe2}) \rightarrow d(\text{Fe2})$ transitions combined with a small amount of $d(\text{Fe1}) \rightarrow d(\text{Fe1})$ transitions. This is in agreement with the fact that upon reduction of the ferric–ferric cluster, the Fe2 ion becomes more reduced than the Fe1 ion, as revealed by the charge density difference shown in Figure 2b. The lowest energy absorption from the ground to the first excited state is contributed by the local excitation between two split e band d-orbitals of the ferrous iron (Fe2) due to the distorted tetrahedral environment. The small energy splitting of 0.04 eV (about 300 cm^{-1}) is in line with the observed energy splitting (400 cm^{-1}) for the ferrous iron in spinach and parsley ferredoxins estimated from fitting to Mössbauer spectra.^{7,8} Further, according to Figure S6, the dominant contributions to the TCDs of the second band of excited states for the ferric–ferrous dimer come from charge-transfer d–d excitations between the ferrous and ferric Fe ions. This is also quite different in nature from the low-lying excited states of the homovalent dimer.

Simulated Spectra for Iron–Sulfur Dimers. We simulated the SXRS S_{SXRS} and absorption spectra S_L in X, Y, and Z polarized light for an oriented (e.g., in solid phase) iron–sulfur cluster; see Figure 3. Figure 3a depicts the normalized spectra of the $[\text{2Fe(III,III)}-2\text{S}]$ dimer, covering a spectral range from 2.06–3.18 eV (corresponding wavelength of 601–389 nm). The two spectra show significant differences for the Y polarization but are almost identical for X and Z polarizations. This feature indicates that both absorption and SXRS spectra are dependent on the incoming pulse directions. The absorption almost exclusively spans the 2.2–2.4 eV regime whereas the SXRS spans the 2.9–3.1 eV regime. We find significant enhancements in the SXRS for the 6th, 7th, 13th, 15th, and 16th excited states compared to the absorption. The relative enhancements in SXRS indicates that this technique may allow a better observation of dark states in the absorption. The separation of the absorption-active (2.2–2.4 eV) and the Raman-active (2.9–3.1 eV) states should allow for the selective excitation of excited states by properly tuning the excitation

bandwidth. The ensuing electronic dynamics may then report on the initial electronic superposition and be sensitive to the biochemical environment.

Figure 3b depicts the normalized S_{SXRS} and S_{L} spectra of the Fe(III)–Fe(II) dimer, spanning the 0.04–2.31 eV spectral range (corresponding wavelength of 31 μm to 536 nm). Note that the low-energy excitation peaks are stronger than those in the visible range in the Y and Z polarizations. While the S_{SXRS} and S_{L} spectra for the second band of excited states are quite similar, there are significant differences for the first band of excited states in the Y direction. The second and fourth states are almost exclusively observed in the absorption, while the fifth, seventh, and eighth excited states by the Raman excitation in Y polarization. Besides, it is noted that the low energy d–d transitions enable the absorption at longer wavelength light from near-infrared (0.78 eV, 1550 nm) down to the mid infrared (microwave) regime (0.04 eV, 31 μm). In reality, however, the low-energy part of the electronic spectrum and the vibrational spectrum may overlap. This highlights the need for a quantum calculation of a vibronic spectrum, with a proper treatment of molecular vibrations, in the iron–sulfur complexes. Finally, we emphasize that the spectrum around 2 eV is qualitatively different from that for the ferric–ferric dimer, indicating the different natures of excited states of these two complexes within the same energy regime.

In conclusion, we employed the high-level *ab initio* DMRG algorithm to calculate the low-lying electronic states of [2Fe–2S] dimers in different oxidation states. Consistent with earlier proposals, the reduced dimer exhibits very low-energy electronic excitations below visible wavelengths. Using the excited states and the transition charge densities, we simulated the off-resonant SXRS and absorption spectra of the dimers. We find significant differences in spectral intensity between the absorption-active and the Raman-active states of the iron–sulfur dimers along one of the axes of incidence, providing a novel means to access previously dark states. This difference in spectral intensity also allows for the selective excitation of excited states by a proper tuning of the excitation bandwidth, thus probing different types of dynamics following the preparation of an initial electronic superposition. This will be a topic of future work.

■ ASSOCIATED CONTENT

■ Supporting Information

The Supporting Information is available free of charge on the ACS Publications website at DOI: 10.1021/acs.jpclett.9b02414.

Additional computational details and results including (1) active orbitals, (2) charge density differences between excited states and the ground state, (3) transition charge densities, and (4) natural transition orbitals for each excited state of the two iron–sulfur dimers (PDF)

■ AUTHOR INFORMATION

Corresponding Authors

*E-mail: daeheimc@uci.edu.

*E-mail: smukamel@uci.edu.

*E-mail: gkc1000@gmail.com.

*E-mail: zhendongli2008@gmail.com.

ORCID

Daeheum Cho: 0000-0002-0322-4291

Jeremy R. Rouxel: 0000-0003-3438-6370

Shaul Mukamel: 0000-0002-6015-3135

Zhendong Li: 0000-0002-0683-6293

Notes

The authors declare no competing financial interest.

■ ACKNOWLEDGMENTS

S.M. gratefully acknowledges the support of the National Science Foundation (grant CHE1663822) and the Chemical Sciences, Geosciences, and Biosciences division, Office of Basic Energy Sciences, Office of Science, U.S. Department of Energy through award No. DE-FG02-04ER15571. D.C. was supported by the DOE award. Work performed at Caltech was supported by the US National Science Foundation (CHE1665333). The BLOCK and PySCF programs were developed with the support of the US National Science Foundation (CHE1657286). G.K.C. is a Simons Investigator in Physics. Z.L. acknowledges the Beijing Normal University Startup Package.

■ REFERENCES

- (1) Beinert, H.; Holm, R. H.; Münck, E. Iron-sulfur clusters: nature's modular, multipurpose structures. *Science* **1997**, *277*, 653–659.
- (2) Howard, J. B.; Rees, D. C. Structural basis of biological nitrogen fixation. *Chem. Rev.* **1996**, *96*, 2965–2982.
- (3) Rees, D. C.; Howard, J. B. The interface between the biological and inorganic worlds: iron-sulfur metalloclusters. *Science* **2003**, *300*, 929–931.
- (4) Blumberger, J. Recent advances in the theory and molecular simulation of biological electron transfer reactions. *Chem. Rev.* **2015**, *115*, 11191–11238.
- (5) Palmer, G.; Sands, R. On the magnetic resonance of spinach ferredoxin. *J. Biol. Chem.* **1966**, *241*, 253.
- (6) Brintzinger, H.; Palmer, G.; Sands, R. H. On the ligand field of iron in ferredoxin from spinach chloroplasts and related nonheme iron enzymes. *Proc. Natl. Acad. Sci. U. S. A.* **1966**, *55*, 397.
- (7) Dunham, W. R.; Bearden, A. J.; Salmeen, I. T.; Palmer, G.; Sands, R. H.; Orme-Johnson, W.; Beinert, H. The two-iron ferredoxins in spinach, parsley, pig adrenal cortex, *Azotobacter vinelandii*, and *Clostridium pasteurianum*: studies by magnetic field Mössbauer spectroscopy. *Biochim. Biophys. Acta, Bioenerg.* **1971**, *253*, 134–152.
- (8) Dunham, W. R.; Palmer, G.; Sands, R. H.; Bearden, A. J. On the structure of the iron-sulfur complex in the two-iron ferredoxins. *Biochim. Biophys. Acta, Bioenerg.* **1971**, *253*, 373–384.
- (9) Mayerle, J.; Frankel, R. B.; Holm, R.; Ibers, J. A.; Phillips, W.; Weiher, J. Synthetic Analogs of the Active Sites of Iron-Sulfur Proteins. Structure and Properties of Bis [*o*-xylyl- μ -2-sulfido-ferrate (III)], an Analog of the 2Fe-2S Proteins. *Proc. Natl. Acad. Sci. U. S. A.* **1973**, *70*, 2429–2433.
- (10) Mayerle, J.; Denmark, S. E.; DePamphilis, B.; Ibers, J. A.; Holm, R. Synthetic analogs of the active sites of iron-sulfur proteins. XI. Synthesis and properties of complexes containing the iron sulfide (FeS₂) core and the structures of bis [*o*-xylyl- μ -2-sulfido-ferrate (III)] and bis [*p*-tolylthiolato- μ -2-sulfido-ferrate (III)] dianions. *J. Am. Chem. Soc.* **1975**, *97*, 1032–1045.
- (11) Venkateswara Rao, P.; Holm, R. Synthetic analogues of the active sites of iron-sulfur proteins. *Chem. Rev.* **2004**, *104*, 527–560.
- (12) Girerd, J.-J. Electron transfer between magnetic ions in mixed valence binuclear systems. *J. Chem. Phys.* **1983**, *79*, 1766–1775.
- (13) Noodleman, L.; Baerends, E. J. Electronic structure, magnetic properties, ESR, and optical spectra for 2-iron ferredoxin models by LCAO-X. α . valence bond theory. *J. Am. Chem. Soc.* **1984**, *106*, 2316–2327.

- (14) Noodleman, L. Valence bond description of antiferromagnetic coupling in transition metal dimers. *J. Chem. Phys.* **1981**, *74*, 5737–5743.
- (15) Noodleman, L.; Norman, J. G., Jr; Osborne, J. H.; Aizman, A.; Case, D. A. Models for ferredoxins: electronic structures of iron-sulfur clusters with one, two, and four iron atoms. *J. Am. Chem. Soc.* **1985**, *107*, 3418–3426.
- (16) Yamaguchi, K.; Fueno, T.; Ueyama, N.; Nakamura, A.; Ozaki, M. Antiferromagnetic spin couplings between iron ions in iron- μ_2 -sulfur clusters. A localized picture by the spin vector model. *Chem. Phys. Lett.* **1989**, *164*, 210–216.
- (17) Noodleman, L.; Lovell, T.; Liu, T.; Himo, F.; Torres, R. A. Insights into properties and energetics of iron-sulfur proteins from simple clusters to nitrogenase. *Curr. Opin. Chem. Biol.* **2002**, *6*, 259–273.
- (18) Sharma, S.; Sivalingam, K.; Neese, F.; Chan, G. K.-L. Low-energy spectrum of iron-sulfur clusters directly from many-particle quantum mechanics. *Nat. Chem.* **2014**, *6*, 927–933.
- (19) Chilkuri, V. G.; DeBeer, S.; Neese, F. Ligand Field Theory and Angular Overlap Model Based Analysis of the Electronic Structure of Homovalent Iron–Sulfur Dimers. *Inorg. Chem.* **2019**, DOI: 10.1021/acs.inorgchem.9b00974.
- (20) White, S. R.; Martin, R. L. Ab initio quantum chemistry using the density matrix renormalization group. *J. Chem. Phys.* **1999**, *110*, 4127–4130.
- (21) Chan, G. K.-L.; Head-Gordon, M. Highly correlated calculations with a polynomial cost algorithm: A study of the density matrix renormalization group. *J. Chem. Phys.* **2002**, *116*, 4462–4476.
- (22) Legeza, Ö.; Röder, J.; Hess, B. A. Controlling the accuracy of the density-matrix renormalization-group method: The dynamical block state selection approach. *Phys. Rev. B: Condens. Matter Mater. Phys.* **2003**, *67*, 125114.
- (23) Moritz, G.; Hess, B. A.; Reiher, M. Convergence behavior of the density-matrix renormalization group algorithm for optimized orbital orderings. *J. Chem. Phys.* **2005**, *122*, 024107.
- (24) Sharma, S.; Chan, G. K.-L. Spin-adapted density matrix renormalization group algorithms for quantum chemistry. *J. Chem. Phys.* **2012**, *136*, 124121.
- (25) Van Kuiken, B. E.; Hahn, A. W.; Nayyar, B.; Schiewer, C. E.; Lee, S. C.; Meyer, F.; Weyhermüller, T.; Nicolaou, A.; Cui, Y.-T.; Miyawaki, J.; Harada, Y.; DeBeer, S. Electronic Spectra of Iron–Sulfur Complexes Measured by 2p3d RIXS Spectroscopy. *Inorg. Chem.* **2018**, *57*, 7355–7361.
- (26) Eaton, W. A.; Palmer, G.; Fee, J. A.; Kimura, T.; Lovenberg, W. Tetrahedral iron in the active center of plant ferredoxins and beef adrenodoxin. *Proc. Natl. Acad. Sci. U. S. A.* **1971**, *68*, 3015–3020.
- (27) Gel'mukhanov, F.; Ågren, H. Resonant X-ray Raman scattering. *Phys. Rep.* **1999**, *312*, 87–330.
- (28) Sun, Y.-P.; Liu, J.-C.; Wang, C.-K.; Gel'mukhanov, F. Propagation of a strong x-ray pulse: Pulse compression, stimulated Raman scattering, amplified spontaneous emission, lasing without inversion, and four-wave mixing. *Phys. Rev. A: At., Mol., Opt. Phys.* **2010**, *81*, 013812.
- (29) Weninger, C.; Purvis, M.; Ryan, D.; London, R. A.; Bozek, J. D.; Bostedt, C.; Graf, A.; Brown, G.; Rocca, J. J.; Rohringer, N. Stimulated electronic x-ray Raman scattering. *Phys. Rev. Lett.* **2013**, *111*, 233902.
- (30) Weninger, C.; Rohringer, N. Stimulated resonant x-ray Raman scattering with incoherent radiation. *Phys. Rev. A: At., Mol., Opt. Phys.* **2013**, *88*, 053421.
- (31) Dorfman, K. E.; Bennett, K.; Mukamel, S. Detecting electronic coherence by multidimensional broadband stimulated x-ray Raman signals. *Phys. Rev. A: At., Mol., Opt. Phys.* **2015**, *92*, 023826.
- (32) Biggs, J. D.; Zhang, Y.; Healion, D.; Mukamel, S. Watching energy transfer in metalloporphyrin heterodimers using stimulated X-ray Raman spectroscopy. *Proc. Natl. Acad. Sci. U. S. A.* **2013**, *110*, 15597–15601.
- (33) Kroll, T.; et al. Resonant inelastic X-ray scattering on ferrous and ferric bis-imidazole porphyrin and cytochrome c: nature and role of the axial methionine–Fe bond. *J. Am. Chem. Soc.* **2014**, *136*, 18087–18099.
- (34) Van Kuiken, B. E.; Hahn, A. W.; Maganas, D.; DeBeer, S. Measuring Spin-Allowed and Spin-Forbidden d–d Excitations in Vanadium Complexes with 2p3d Resonant Inelastic X-ray Scattering. *Inorg. Chem.* **2016**, *55*, 11497–11501.
- (35) Maganas, D.; DeBeer, S.; Neese, F. A Restricted Open Configuration Interaction with Singles Method To Calculate Valence-to-Core Resonant X-ray Emission Spectra: A Case Study. *Inorg. Chem.* **2017**, *56*, 11819–11836.
- (36) Chernyak, V. Y.; Saurabh, P.; Mukamel, S. Non-linear non-local molecular electrodynamics with nano-optical fields. *J. Chem. Phys.* **2015**, *143*, 164107.
- (37) Anderson, P. W.; Hasegawa, H. Considerations on double exchange. *Phys. Rev.* **1955**, *100*, 675.
- (38) Veryazov, V.; Malmqvist, P. Å.; Roos, B. O. How to select active space for multiconfigurational quantum chemistry? *Int. J. Quantum Chem.* **2011**, *111*, 3329–3338.
- (39) Pinjari, R. V.; Delcey, M. G.; Guo, M.; Odelius, M.; Lundberg, M. Cost and sensitivity of restricted active-space calculations of metal L-edge X-ray absorption spectra. *J. Comput. Chem.* **2016**, *37*, 477–486.
- (40) Presti, D.; Stoneburner, S. J.; Truhlar, D. G.; Gagliardi, L. Full Correlation in a Multiconfigurational Study of Bimetallic Clusters: Restricted Active Space Pair-Density Functional Theory Study of [2Fe-2S] Systems. *J. Phys. Chem. C* **2019**, *123*, 11899.
- (41) Li, Z.; Guo, S.; Sun, Q.; Chan, G. K. Electronic landscape of the P-cluster of nitrogenase as revealed through many-electron quantum wavefunction simulations. *Nat. Chem.* **2019**, DOI: 10.1038/s41557-019-0337-3.
- (42) Pipek, J.; Mezey, P. G. A fast intrinsic localization procedure applicable for abinitio and semiempirical linear combination of atomic orbital wave functions. *J. Chem. Phys.* **1989**, *90*, 4916–4926.
- (43) Becke, A. D. Density-functional exchange-energy approximation with correct asymptotic behavior. *Phys. Rev. A: At., Mol., Opt. Phys.* **1988**, *38*, 3098.
- (44) Perdew, J. P. Density-functional approximation for the correlation energy of the inhomogeneous electron gas. *Phys. Rev. B: Condens. Matter Mater. Phys.* **1986**, *33*, 8822.
- (45) Liu, W. Ideas of relativistic quantum chemistry. *Mol. Phys.* **2010**, *108*, 1679–1706.
- (46) Saue, T. Relativistic Hamiltonians for chemistry: a primer. *ChemPhysChem* **2011**, *12*, 3077–3094.
- (47) Peng, D.; Reiher, M. Exact decoupling of the relativistic Fock operator. *Theor. Chem. Acc.* **2012**, *131*, 1081.
- (48) Li, Z.; Xiao, Y.; Liu, W. On the spin separation of algebraic two-component relativistic Hamiltonians. *J. Chem. Phys.* **2012**, *137*, 154114.
- (49) Balabanov, N. B.; Peterson, K. A. Systematically convergent basis sets for transition metals. I. All-electron correlation consistent basis sets for the 3 d elements Sc–Zn. *J. Chem. Phys.* **2005**, *123*, 064107.
- (50) Sun, Q.; Berkelbach, T. C.; Blunt, N. S.; Booth, G. H.; Guo, S.; Li, Z.; Liu, J.; McClain, J. D.; Sayfutyarova, E. R.; Sharma, S.; Wouters, S.; Chan, G. K. PySCF: the Python-based simulations of chemistry framework. *Wiley Interdiscip. Rev. Comput. Mol. Sci.* **2018**, *8*, e1340.
- (51) Matsika, S.; Feng, X.; Luzanov, A. V.; Krylov, A. I. What we can learn from the norms of one-particle density matrices, and what we can't: Some results for interstate properties in model singlet fission systems. *J. Phys. Chem. A* **2014**, *118*, 11943–11955.
- (52) Hu, W.; Chan, G. K.-L. Excited-state geometry optimization with the density matrix renormalization group, as applied to polyenes. *J. Chem. Theory Comput.* **2015**, *11*, 3000–3009.
- (53) Ren, J.; Peng, Q.; Zhang, X.; Yi, Y.; Shuai, Z. Role of the Dark 2Ag State in Donor–Acceptor Copolymers as a Pathway for Singlet Fission: A DMRG Study. *J. Phys. Chem. Lett.* **2017**, *8*, 2175–2181.
- (54) Martin, R. L. Natural transition orbitals. *J. Chem. Phys.* **2003**, *118*, 4775–4777.

(55) Malmqvist, P. Å.; Veryazov, V. The binatural orbitals of electronic transitions. *Mol. Phys.* **2012**, *110*, 2455–2464.

Supporting Information

Stimulated X-ray Raman and Absorption Spectroscopy of Iron-Sulfur Dimers

Daeheum Cho,^{*,†} Jeremy R. Rouxel,[†] Shaul Mukamel,^{*,†} Garnet Kin-Lic Chan,^{*,‡}
and Zhendong Li^{*,¶}

[†]*Department of Chemistry and Physics and Astronomy, University of California, Irvine,
California 92697-2025, USA*

[‡]*Division of Chemistry and Chemical Engineering, California Institute of Technology,
Pasadena, CA 91125, USA*

[¶]*Division of Chemistry and Chemical Engineering, California Institute of Technology,
Pasadena, CA 91125, USA,*

*Key Laboratory of Theoretical and Computational Photochemistry, Ministry of Education,
College of Chemistry, Beijing Normal University, Beijing 100875, China*

E-mail: daeheimc@uci.edu; smukamel@uci.edu; gkc1000@gmail.com;
zhendongli2008@gmail.com

Contents

1	Active space of [2Fe-2S] dimers	3
2	Charge density difference	4
3	Transition charge densities	6
4	Binatural/Natural transition orbitals	7

1 Active space of [2Fe-2S] dimers

The 36 active orbitals are shown in Fig. 1. They can be classified as follows: 1-8 (terminal S), 9-14 (bridge S), 15-24 (3d of Fe), and 25-36 (4s or 4d of Fe).

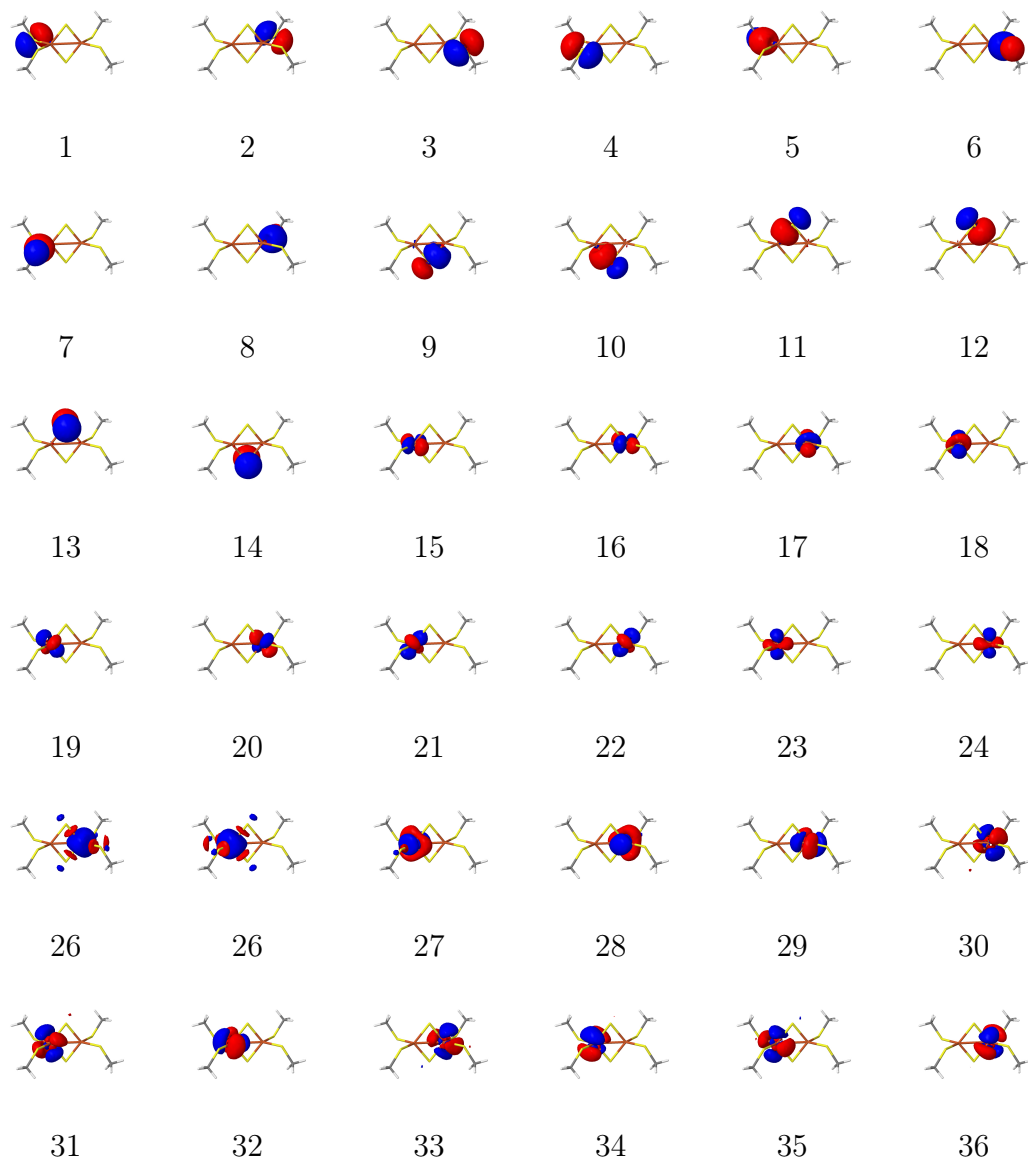


Figure 1: Active orbitals of [2Fe-2S] dimers.

2 Charge density difference

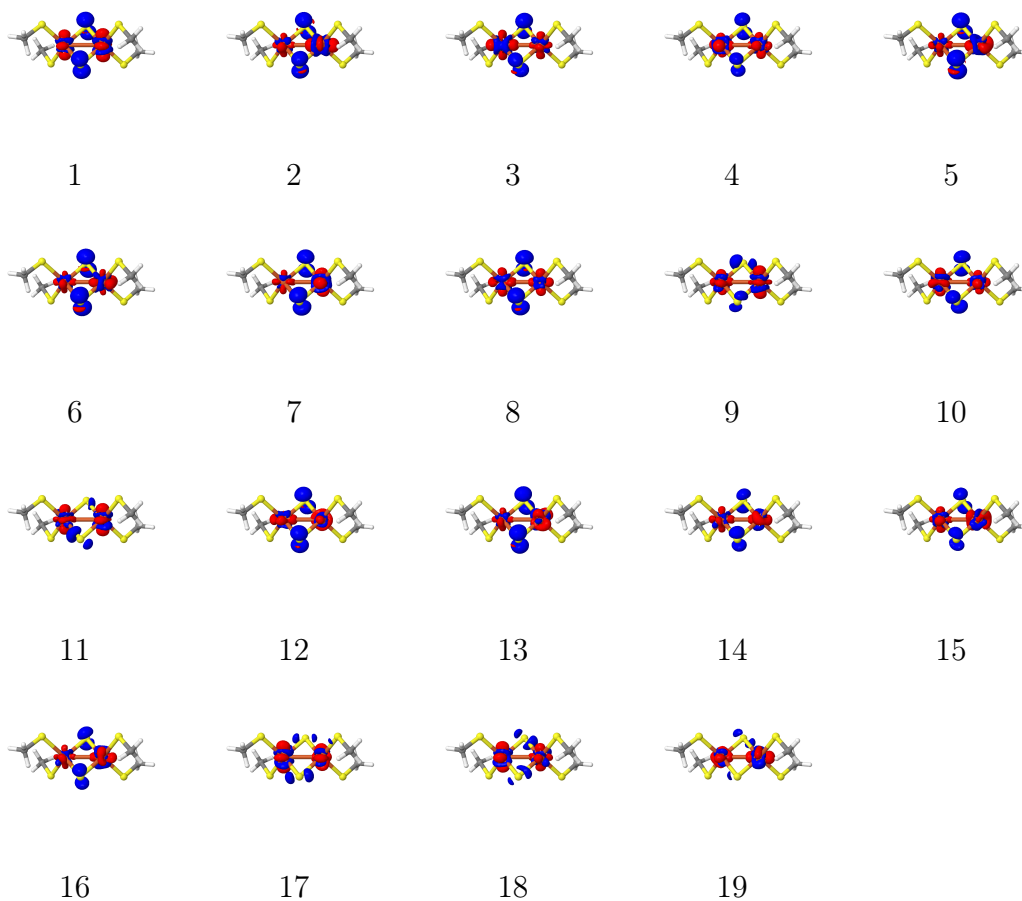


Figure 2: Charge density difference between excited states ($S = 0$) and the ground state of the $[2\text{Fe(III,III)}-2\text{S}]$ complex

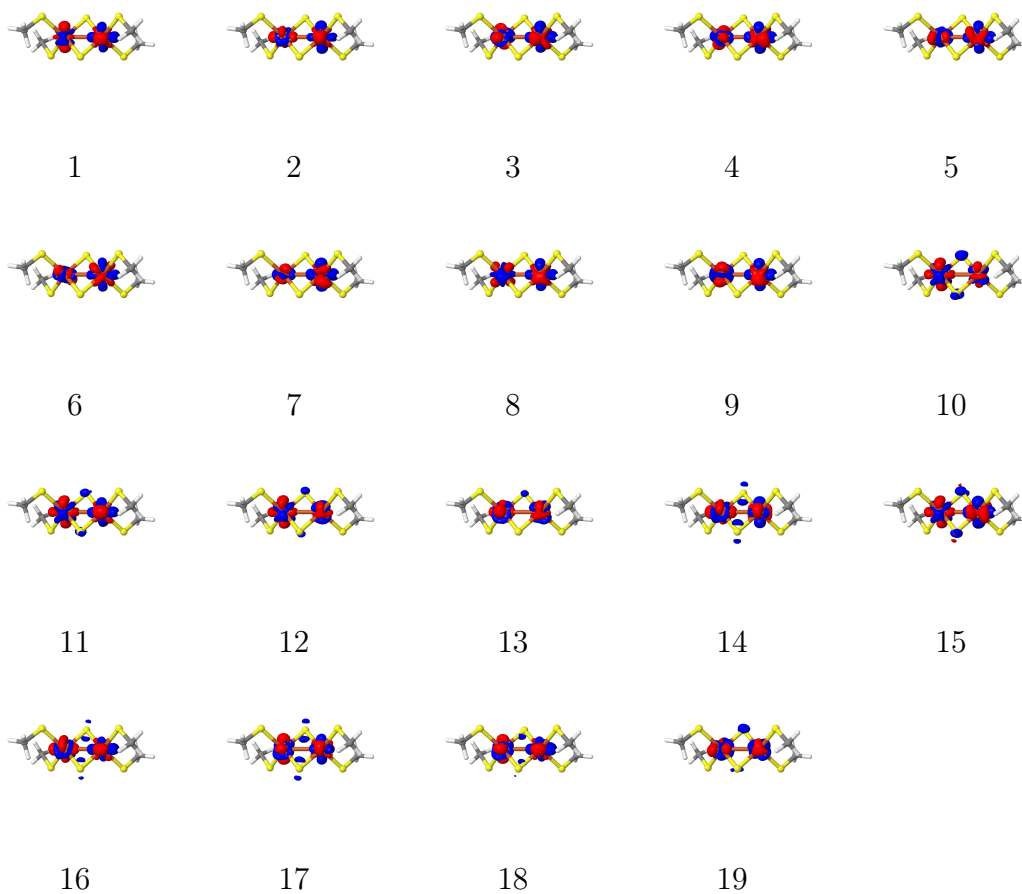


Figure 3: Charge density difference between excited states ($S = 1/2$) and the ground state of the [2Fe(III,II)-2S] complex.

3 Transition charge densities

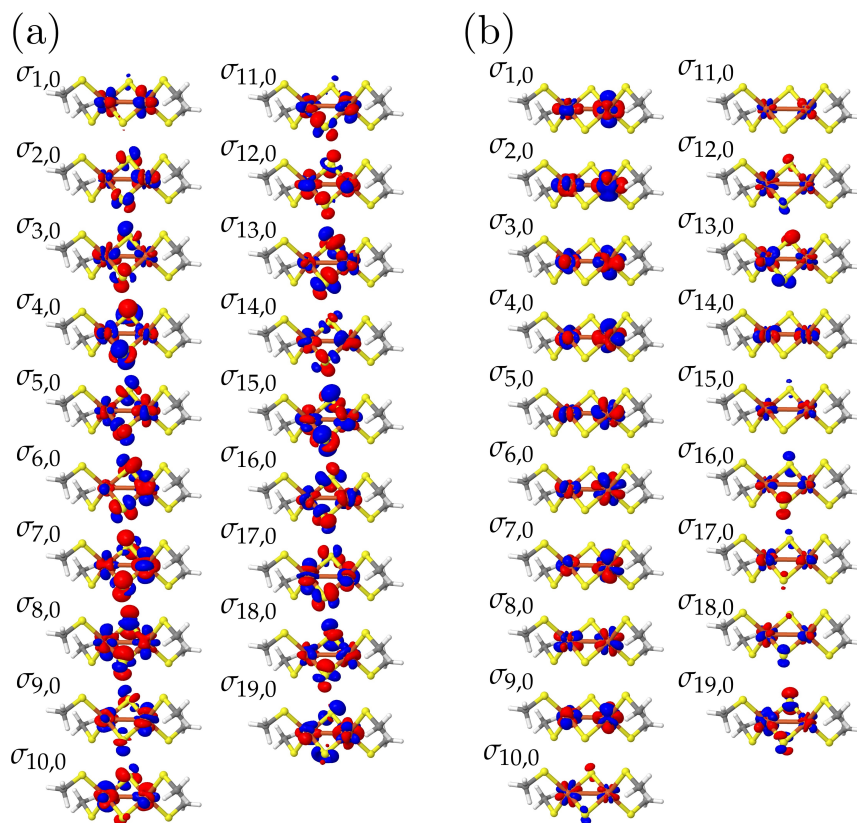


Figure 4: Transition charge density of respective electronic excitations of (a) the [2Fe(III,III)-2S] complex and (b) the [2Fe(III,II)-2S] complex.

4 Binatural/Natural transition orbitals

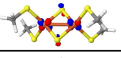
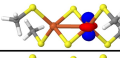
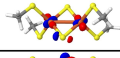
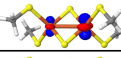
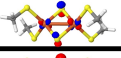
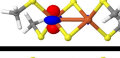
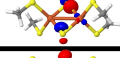
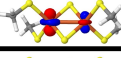
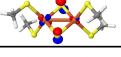
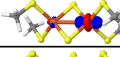
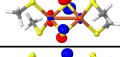
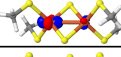
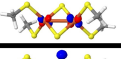
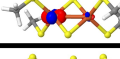
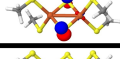
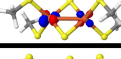
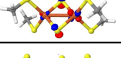
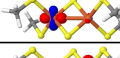
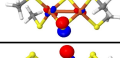
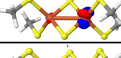
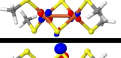
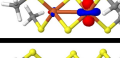
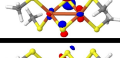
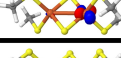
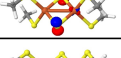
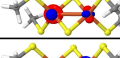
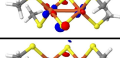
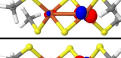
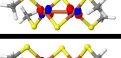
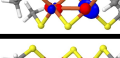
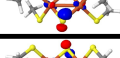
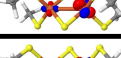
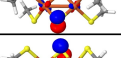
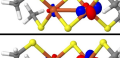
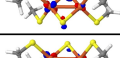
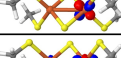
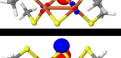
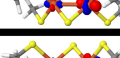
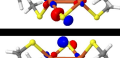
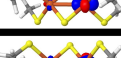
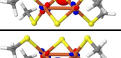
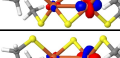
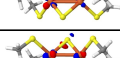
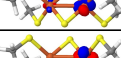
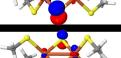
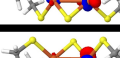
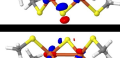
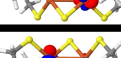
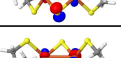
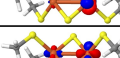
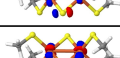
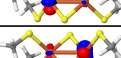
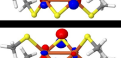
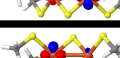
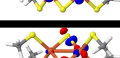
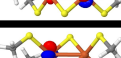
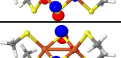
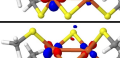
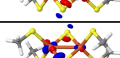
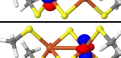
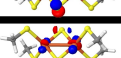
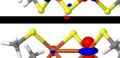
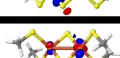
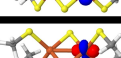
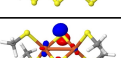
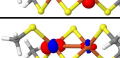
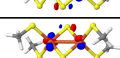
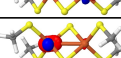
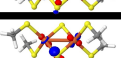
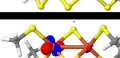


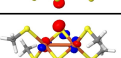
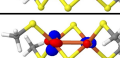


		HNTO	ENTO	Contrib.			HNTO	ENTO	Contrib.
S_1	1			0.642	S_{11}	1			0.711
	2			0.300		2			0.168
S_2	1			0.921	S_{12}	1			0.372
	2			0.069		2			0.264
S_3	1			0.865	S_{13}	1			0.469
	2			0.115		2			0.411
S_4	1			0.616	S_{14}	1			0.310
	2			0.229		2			0.273
S_5	1			0.461	S_{15}	1			0.411
	2			0.396		2			0.241
S_6	1			0.471	S_{16}	1			0.364
	2			0.450		2			0.321
S_7	1			0.710	S_{17}	1			0.743
	2			0.111		2			0.186
S_8	1			0.423	S_{18}	1			0.610
	2			0.250		2			0.218
S_9	1			0.657	S_{19}	1			0.458
	2			0.133		2			0.197
S_{10}	1			0.393					
	2			0.324					

Figure 5: Two dominant sets of HNTOs and ENTOS of respective electronic excitations of the $[2\text{Fe(III,III)}-2\text{S}]$ complex.

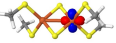
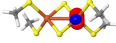
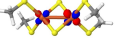
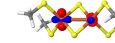
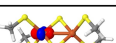
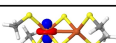
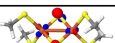
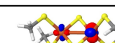
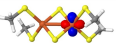
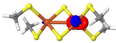
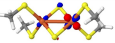
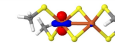
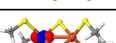
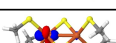
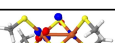
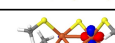
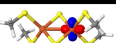
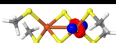
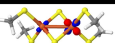

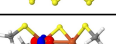
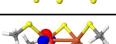
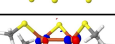
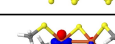
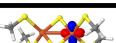
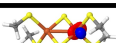
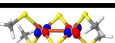
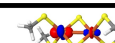
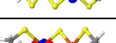
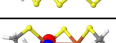
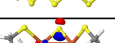
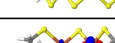
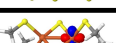
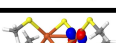
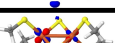
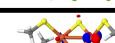
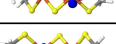
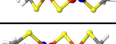
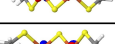
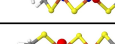
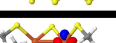
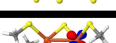
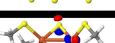
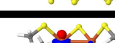
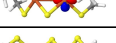
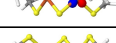

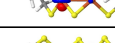
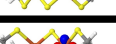
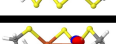
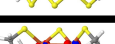
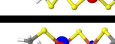
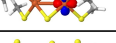
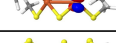
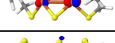
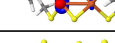
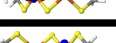
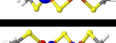
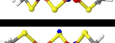

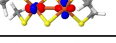
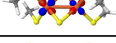
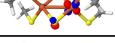
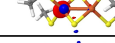
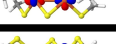
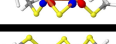
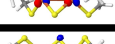
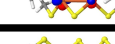
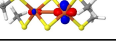
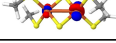
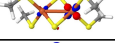
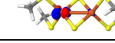
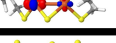
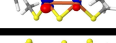
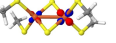
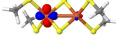
		HNTOs	ENTOs	Contrib.			HNTOs	ENTOs	Contrib.
D_1	1			0.811	D_{11}	1			0.662
	2			0.179		2			0.312
D_2	1			0.786	D_{12}	1			0.903
	2			0.156		2			0.083
D_3	1			0.814	D_{13}	1			0.884
	2			0.167		2			0.097
D_4	1			0.874	D_{14}	1			0.776
	2			0.114		2			0.132
D_5	1			0.833	D_{15}	1			0.580
	2			0.165		2			0.302
D_6	1			0.914	D_{16}	1			0.525
	2			0.085		2			0.386
D_7	1			0.933	D_{17}	1			0.858
	2			0.065		2			0.086
D_8	1			0.674	D_{18}	1			0.558
	2			0.322		2			0.339
D_9	1			0.749	D_{19}	1			0.900
	2			0.241		2			0.070
D_{10}	1			0.911					
	2			0.078					

Figure 6: Two dominant sets of HNTOs and ENTOS of respective electronic excitations of the $[2\text{Fe(III,II)}]\text{-2S}$ complex.